Computational design optimization for microfluidic magnetophoresis

Brian D. Plouffe, Laura H. Lewis, and Shashi K. Murthy[a)]
Department of Chemical Engineering, Northeastern University, Boston, Massachusetts 02115, USA

(Received 6 December 2010; accepted 11 January 2011; published online 30 March 2011)

Current macro- and microfluidic approaches for the isolation of mammalian cells are limited in both efficiency and purity. In order to design a robust platform for the enumeration of a target cell population, high collection efficiencies are required. Additionally, the ability to isolate pure populations with minimal biological perturbation and efficient off-chip recovery will enable subcellular analyses of these cells for applications in personalized medicine. Here, a rational design approach for a simple and efficient device that isolates target cell populations via magnetic tagging is presented. In this work, two magnetophoretic microfluidic device designs are described, with optimized dimensions and operating conditions determined from a force balance equation that considers two dominant and opposing driving forces exerted on a magnetic-particle-tagged cell, namely, magnetic and viscous drag. Quantitative design criteria for an electromagnetic field displacement-based approach are presented, wherein target cells labeled with commercial magnetic microparticles flowing in a central sample stream are shifted laterally into a collection stream. Furthermore, the final device design is constrained to fit on standard rectangular glass coverslip (60 (L) $\times$ 24 (W) $\times$ 0.15 (H) mm^3) to accommodate small sample volume and point-of-care design considerations. The anticipated performance of the device is examined via a parametric analysis of several key variables within the model. It is observed that minimal currents ($<$500 mA) are required to generate magnetic fields sufficient to separate cells from the sample streams flowing at rate as high as 7 ml/h, comparable to the performance of current state-of-the-art magnet-activated cell sorting systems currently used in clinical settings. Experimental validation of the presented model illustrates that a device designed according to the derived rational optimization can effectively isolate ($\sim$100%) a magnetic-particle-tagged cell population from a homogeneous suspension even in a low abundance. Overall, this design analysis provides a rational basis to select the operating conditions, including chamber and wire geometry, flow rates, and applied currents, for a magnetic-microfluidic cell separation device. © *2011 American Institute of Physics.* [doi:10.1063/1.3553239]

I. INTRODUCTION

The separation of a pure cell population from heterogeneous suspensions is a vital step that precedes analytical or diagnostic characterization of biological samples. The separation of key cell populations, such as circulating tumor cells[1] and endothelial progenitor cells,[2] can provide valuable insight into the prognosis and progression of certain diseases. Additionally, gaining this information in a minimally invasive fashion, such as through analysis of a blood sample, reduces the need for biopsies and invasive surgeries.

Cell separation techniques may be broadly classified into two categories: those based on size

[a)]Author to whom correspondence should be addressed. Electronic mail: smurthy@coe.neu.edu.

and density and those based on affinity (chemical, electrical, or magnetic).[3] Techniques that achieve separation based on size and density are generally unable to provide adequate resolution between cell populations known to be of similar size.[3] Affinity-based approaches, such as cell adhesion chromatography[4,5] and dielectrophoresis,[6] are alternative methods to separate cell populations, but these techniques are still limited in the efficiency and purity of cell capture.[3,7] Furthermore, once target cells are isolated, recovery of viable cells for further application remains a challenge.[8] Another affinity-based technique is fluorescence activated cell sorting, where antibodies tagged with fluorescent dyes are attached to cells in mixed suspensions via receptor-ligand binding. These cells are then sorted individually based on their fluorescence and light scattering properties. Although this technique can provide highly pure (95% or higher) cell populations, it requires expensive equipment and has limited throughput ($\sim 10^7$ cells/h).[9]

Magnetic particles functionalized with ligands can be utilized to tag and subsequently facilitate separation of cells associated with disease conditions, such as circulating tumor cells,[1] endothelial progenitor cells,[10] and lymphocyte subpopulations.[11–13] The technique of magnet-activated cell sorting (MACS) allows target cell separation to be carried out in parallel, providing rapid separation ($\sim 10^{11}$ cells/h) of high-purity cell populations.[14] However, operation of commercially available MACS systems requires many processing steps, including several preprocessing and washing procedures, rendering it a very time-consuming batchwise procedure.[15] To overcome some of these limitations, techniques based on continuous-flow separation of magnetically tagged cell have been investigated.[16,17] These analytical tools are typically bulky and require large volumes of sample (>5 ml) for operation.[17] The advancement of MACS technology over the last 5–10 years has focused on miniaturization of the continuous-flow analysis chambers to the micron scale.[18–23] These microscale fluidic devices, or microfluidic channels, allow for the analysis of significantly smaller sample volumes while maintaining comparable purity of target cells within the collection suspension. Nonetheless, the current state-of-the-art in microfluidic MACS technology is still limited in throughput in comparison to other continuous-flow methods. Moreover, these microfluidic MACS designs are often based on Edisonian methods of device design arrived at after multiple operational iterations rather than from rational design derived from a systematic physical approach.

The methodology described in this work applies a rational computational design approximation to the development of a magnetophoretic cell isolation chamber. In contrast to prior microfluidic designs that employ static magnetic separation,[24] adhesion-based separation[25] or dielectrophoresis technology,[26] this work describes a continuous-flow, magnetic displacement-based design, wherein cells labeled with magnetic particle tags are separated from a sample stream under the influence of a magnetic field without mechanical disruption and/or postprocess analysis (e.g., immunohistochemical identification or colony-form unit assays). The applied magnetic field of this rational design is generated by an integrated electromagnet (current-carrying wire) located below the microfluidic channel. Electromagnets have two distinct advantages over designs that utilize permanent magnets:[21–23,27] first, they can be easily switched on/off to facilitate cell capture and release, and second the strength of the resultant magnetic field may be tuned by varying current. In the microfluidic device context, electromagnets have seen limited use because they typically produce weak magnetic fields and they generally require at least two steps of lithography that must be repeated in the fabrication of each device. In addition, bulkiness of the electromagnet and potential Joule heating derived from large currents flowing through the electromagnet coil can quickly become problematic.[27] The device design described in this paper addressed these limitations by creating a new microfluidic device design derived from first-principles and rational design parameters.

As the ultimate aim of the device described herein is for application in diagnostic and regenerative medicine, additional constraints and conditions exist that need to be addressed within the model. Point-of-care diagnostic devices typically utilize a biological fluid sample analyte, such as blood, interstitial fluid, saliva, vaginal fluid or cellular material, or nasal fluid. As a means of minimizing contact with the analyst, or of contaminating further tests, the microfluidic chamber should be disposable.[28,29] Thus, it is desirable to separate the microfluidic component of this

system from the reusable electromagnetic components of the design. In addition to addressing biohazard considerations, this arrangement will significantly reduce cost associated with device manufacture and implementation.

In contrast to prior models of continuous-flow magnetic-microfluidic separation devices,[30,31,24,32] the specific advance articulated in this paper is the development and implementation of a realistic rational design based on practical experimental constraints and desired need for a microfluidic system capable of delivering both high efficiency and high purity. The described approach directly accounts for variations in key parameters within the cells, tagging particles, and device and addresses several key parameters, which may advance this device to clinical and bench-top applications. Although many modeling approaches have been well established in literature,[30,31,24,32] these examples fail to address all of the requirements of a clinically usable cell separation platform. The magnet-based cell separation device presented here aims to incorporate clinical diagnostic considerations *ab initio* by constraining the device microfluidic channel dimensions to a practical scale (i.e., that of a microscope slide) and incorporating disposable and nondisposable components (fluidic and magnetic parts, respectively) in the device as a means of reducing cost. Furthermore, the incorporation of a tunable electromagnet (relative to state-of-the-art on-chip designs that employ permanent magnets[30,32]) maximizes versatility in addition to reducing device cost. In addition, the design presented here accounts for drag forces experienced by cells tagged with hundreds of magnetic beads. This approach is more realistic for continuous-flow cell separation compared to that described by prior theoretical/computational models that only consider the manipulation of magnetic micro- or nanoparticles in the absence of cell attachment,[30,24,32] as cells are generally much larger in size relative to the particles. The device model described here also introduces a new and unique sheath-based design in which a system of two electromagnets acts cooperatively to displace cells within a central microfluidic channel.

In this work, two magnetophoretic microfluidic device designs are presented (denoted as generation I and generation II, respectively) with optimized dimensions and operating conditions. Both designs were constrained to the dimensions of standard rectangular glass coverslip ($60\ \text{(L)} \times 24\ \text{(W)} \times 0.15\ \text{(H)}\ \text{mm}^3$). While ultimately the generation I design proved to be ineffective in achieving the stated device design goals, it is included in this work as it serves as a useful illustration of the analytical derivation of the equation of motion of magnetically tagged cells in microfluidic channel. Moreover, the successful generation II device design makes use of the force balances developed for the generation I device design. These two designs were determined by computational efforts based on a force balance equation that considers the two driving forces exerted on a magnetically tagged cell moving through a Newtonian liquid. The main forces considered are the magnetic forces $\vec{F}_m$ originating from a current-carrying wire located adjacent to the device to draw a tagged particle toward a desired location and the Stokes force $\vec{F}_s$ that opposes the motion of the particle. The variables associated with the described derivations are listed in the Nomenclature section. To attain a more realistic device design, an experimental analysis of several of the key parameters associated with magnetophoretic devices was performed (i.e., magnetic particle and cell properties and cell-particle-binding characteristics) and directly accounted for in the resulting computation. In the course of this investigation, it was determined that the generation I (single-wire) device design was not feasible as it yielded significantly inferior particle deflection as compared to that provided by the generation II (dual-wire/fluid sheath) device design. Several different width (generation II) designs were fabricated and experimentally validated against the derived optimization, whereas applied current and flow rates were tuned and compared with the rational design, as to provide a functional cell separation platform. To the best of the authors' knowledge, the work presented here constitutes the first rationally derived magnetophoretic microfluidic device designs in the open literature, and future efforts will be devoted to synthesizing and testing the computational cell trajectories in both heterogeneous cell suspension in Newtonian fluids (e.g., saline) and non-Newtonian fluids (e.g., whole blood).

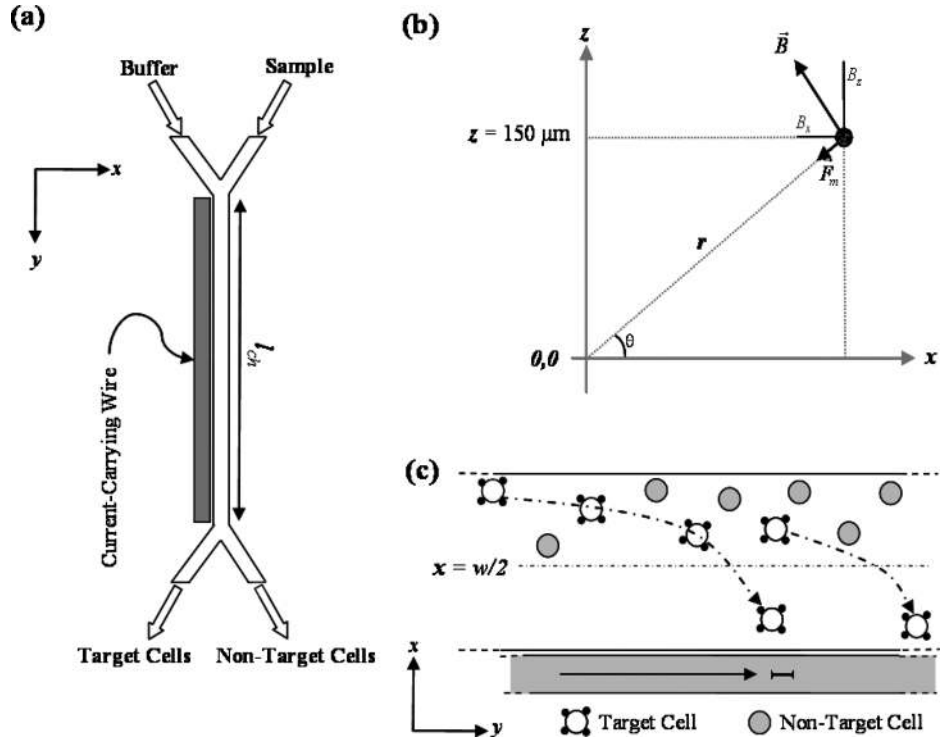

FIG. 1. Schematic illustration of the generation I cell separation device design: (a) buffer stream is injected on the side closest to current-carrying wire and sample stream injected to the far-side with respect to the current-carrying wire. The device length required for the target cell to displace from the sample stream to the buffer stream is l_{ch}. (b) Mathematical configuration of single current-carrying wire located at (0,0) with current flowing in the positive y-direction (out of the page). The particle positioned at height above of the wire (z=150 μm) and distance away (x) from the current-carrying wire. The magnetic force vector ($\vec{F}_m$) perpendicular to direction of the magnetic field vector ($\vec{B}$). [(a) and (c)] The generation I cell separation device displaces target cells from sample stream to buffer stream; nontarget cells remain in sample stream. The distance required for complete displacement of target cells from the far-edge to interface of the sample and buffer streams is half the width of the device (x=w/2).

II. DEVICE GEOMETRIES

This section describes the geometrical layout of the two microfluidic chambers investigated in this paper. In both cases, the analyte is a heterogeneous cell suspension containing cells tagged with magnetic particles in addition to nontarget cells. The design objective is to displace the target population from the mixed suspension in continuous flow. The first-generation design (generation I) incorporates a single current-carrying wire of rectangular cross section located adjacent to the microfluidic channel (Fig. 1). The generated magnetic field deflects the cell-particle complex within the biological fluid sample, which is initially located at the far-side with respect to the wire, toward the buffer stream, which is at the near-side [Figs. 1(a) and 1(c)]. The current-carrying wire is located below the microchannel and is separated from the fluidic separation channel to minimize fabrication costs (only the fluidic component needs replacement with each analysis); the wire and support may be reused for subsequent samples. This design feature requires the flow channel of the microfluidic device, and hence the cell-particle complexes within the channel, to be raised up by the thickness of a glass coverslip, or approximately 150 μm, above the current-carrying wire in the vertical ($\hat{z}$) direction (perpendicular to the plane of the chamber), as shown in Fig. 1(b).

The incorporation of a second conducting wire in parallel alignment with the first wire allows tagged-cell displacement in both positive and negative lateral ($\hat{x}$) directions toward a center stream of buffer. This design, designated as generation II, reduces the displacement distance required for cell isolation by increasing the magnetic forces experienced by the cell-particle complex. As shown in Fig. 2, the current-carrying wires of the generation II device are located equidistant from

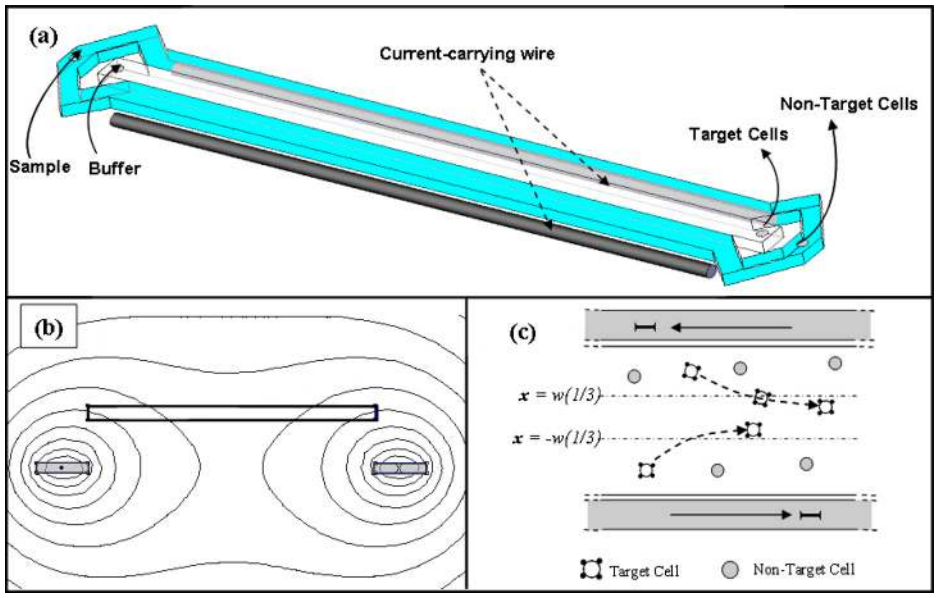

FIG. 2. Schematic illustration of the generation II cell separation design: (a) injected sample split into two streams that sheath central buffer stream (c). (b) Cross-sectional illustration of magnetic flux lines resulting from antiparallel dual-wire configuration driving cell-particle complexes to the middle of the device; here, the central rectangle represents fluid flow channel and shaded rectangles current-carrying wires.

the center of the flow channel and the two currents are assumed to run antiparallel in the $\hat{y}$-direction, parallel to the fluidic flow of the chamber. Here again, the microfluidic device is separated from the current-carrying wire array by a vertical distance of approximately 150 μm.

III. THEORETICAL FORMULATION: FORCES ON THE CELL-PARTICLE COMPLEX

This section describes the derivation of an expression for the displacement of a magnetic particle in a channel subjected to both magnetic $\vec{F}_m$ and Stokes $\vec{F}_s$ forces. The magnetic force and the Stokes force contributions are considered separately; note that gravity and buoyancy forces are negligible and are thus not considered here. The effect of Joule heating is also considered in this section. Prior to derivation of the expected cell displacement under these two driving forces, the potential role of diffusion was examined. Using the Stokes–Einstein relation,[33] $D_{AB} = k_B T / 6\pi\eta R_c$, and the random walk theory for displacement in one dimension,[34] $\Delta x \approx (2D_{AB}t)^{0.5}$, the diffusivity (D_{AB}) of an average cell in buffer can be derived as well as the transverse displacement (Δx) within the microfluidic device. It can be shown that a cell would have a diffusive constant (D_{AB}) on the order of 10^{-15} m^2 s^{-1} at room temperature. Assuming a channel with dimensions of 5 (L) $\times$ 0.2 (W) $\times$ 0.05 (H) cm and a suspension flow rate of 10 μl min^{-1}, the residence time (t) of a cell within the channel is 2.5 min, with lateral (Δx) diffusion of less than 300 nm. Therefore, it was concluded that the effect of diffusion may be ignored within the described design.

A. Magnetic force determination

The trajectory of a magnetically labeled cell in the proposed microfluidic device is modeled by evaluating the forces on the cell generated by motion through the fluid under the attractive action of a magnetic field. Prior to derivation of forces on a cell-particle complex, the forces specific to a single magnetic particle are determined. In the following discussion, the particle is initially located at position (x,y,z), subjected to a magnetic field $\vec{B}$ originating from a current-carrying wire at (0,0,0), as shown in Fig. 1(b). The particle is fixed at $z=150$ μm and moves laterally in the $-x$-direction toward the current-carrying wire independent of the y-component.

A single magnetic particle is idealized as a magnetic sphere of uniform moment density. The magnetic force exerted on the particle, $\vec{F}_m=(\vec{m}\cdot\nabla)\vec{B}$, may be evaluated from the total moment on the particle, $\vec{m}=V_p\vec{M}$, which depends on the volume of the particle (V_p) and the volume magnetization $\vec{M}$. Here, $\vec{M}=\Delta\chi\vec{H}$ and $\Delta\chi$ is the volumetric magnetic susceptibility difference between the particle (χ_p) and the surrounding buffered fluid medium (χ_{med}). The overall response of a magnetic particle in a fluid to a magnetic field is then determined by the strength and gradient of the applied magnetic field ($\vec{B}=\mu_0\vec{H}$), yielding[35,36]

$$\vec{F}_m=\frac{V_p\Delta\chi}{\mu_0}(\vec{B}\cdot\nabla)\vec{B}, \tag{1}$$

where μ_0 is the permeability of vacuum equal to $4\pi\times10^{-7}$ T m A^{-1}. It should be noted that a complementary form of this equation can be determined be applying the Maxwell equation $\nabla\times\vec{B}=0$ to the following mathematical identity:

$$\nabla(\vec{B}\cdot\vec{B})=2\vec{B}\times(\nabla\times\vec{B})+2(\vec{B}\cdot\nabla)=2(\vec{B}\cdot\nabla)\vec{B}. \tag{2}$$

Therefore, Eq. (1) can alternatively be expressed as

$$\vec{F}_m=V_p\Delta\chi\nabla\left(\frac{\vec{B}^2}{2\mu_0}\right). \tag{3}$$

Although Eq. (3) is a valuable relationship for visualizing the magnetic force operative in the system, all subsequent $\vec{F}_m$ analyses are derived from relationships expressed in Eq. (1). As the magnetic susceptibility of the surroundings is typically five to six orders of magnitude lower than that of the particles,[27] $\Delta\chi$ is determined primarily by the susceptibility of the particle, χ_p. By way of example, the magnetic susceptibility of phosphate buffer saline is on the order of 10^{-7} and that of blood is on the order of 10^{-6}, while the susceptibility of commercial magnetic oxide particles is generally on the order of 10^0-10^{-1}.[37,38] Furthermore, it should be noted that the magnetic susceptibility of materials commonly used in the construction of a microfluidic channel has also been found to be several orders of magnitude smaller (approximately $10^{-5}-10^{-6}$)[39] than that of the magnetic beads, and thus the effect of the device itself may also be assumed to be negligible in this analysis.

With these considerations, Eq. (1) can then be expanded in explicit form to yield

$$\vec{F}_m=\frac{V_p\chi_p}{\mu_0}(\vec{B}\cdot\nabla)\vec{B}=\frac{V_p\chi_p}{\mu_0}\begin{bmatrix}B_x\dfrac{\partial B_x}{\partial x}+B_y\dfrac{\partial B_x}{\partial y}+B_z\dfrac{\partial B_x}{\partial z}\\ B_x\dfrac{\partial B_y}{\partial x}+B_y\dfrac{\partial B_y}{\partial y}+B_z\dfrac{\partial B_y}{\partial z}\\ B_x\dfrac{\partial B_z}{\partial x}+B_y\dfrac{\partial B_z}{\partial y}+B_z\dfrac{\partial B_z}{\partial z}\end{bmatrix}. \tag{4}$$

The above equation can be simplified by assuming the current-carrying wire located at the side of the device is infinitely long in the $\hat{y}$-direction, thus allowing the spatial derivatives of the magnetic field to vanish

$$\frac{\partial\vec{B}}{\partial y}=0\Rightarrow\left\{\frac{\partial B_x}{\partial y}=0,\quad\frac{\partial B_y}{\partial y}=0,\quad\frac{\partial B_z}{\partial y}=0\right\}. \tag{5}$$

Furthermore, the symmetry of the device design (Sec. II) dictates that there are no off-axis components of the magnetic field gradient,

$$\left\{ \frac{\partial B_y}{\partial x} = 0, \quad \frac{\partial B_y}{\partial z} = 0 \right\}. \tag{6}$$

The first device design (generation I) that was investigated incorporates a single, rectangular current-carrying wire placed at the periphery of the device (Fig. 1). The wire is situated below the microchannel and is kept separate from the fluidic separation channel.

Employing the Biot–Savart law,[40] the magnetic field $\vec{B}$ at a distance (r) from the current-carrying wire can be determined in cylindrical coordinates as

$$\vec{B} = \frac{\mu_0 I}{2\pi r}\hat{\theta}. \tag{7}$$

For a single current-carrying wire located at the origin (0,0,0) in Fig. 1 with current flowing in the positive $\hat{y}$-directions (out of the page), Eq. (7) is explicitly written in Cartesian coordinates as

$$B_x = -\frac{\mu_0 I}{2\pi r}\frac{z}{r} = \frac{\mu_0 I}{2\pi}\frac{z}{x^2+z^2}, \tag{8a}$$

$$B_z = \frac{\mu_0 I}{2\pi r}\frac{x}{r} = \frac{\mu_0 I}{2\pi}\frac{x^2}{x^2+z^2}. \tag{8b}$$

The magnetic force in the tangential direction is provided as

$$F_{m,x} = \frac{V_p \chi_p}{\mu_0}\left[B_x \frac{\partial B_x}{\partial x} + B_z \frac{\partial B_x}{\partial z} \right]. \tag{9}$$

The x- and z-components of the gradient of the magnetic field are listed below

$$\frac{\partial B_x}{\partial x} = \frac{\mu_0 I}{2\pi}\frac{2zx}{[x^2+z^2]^2}, \tag{10a}$$

$$\frac{\partial B_x}{\partial z} = -\frac{\mu_0 I}{2\pi}\frac{x^2-z^2}{[x^2+z^2]^2} \tag{10b}$$

and are substituted back into Eq. (9) to obtain the expression for the magnitude of the magnetic force exerted on a magnetic particle under the above stated conditions,

$$F_{m,x} = -\frac{V_p \chi_p}{\mu_0}\left[\left(\frac{\mu_0 I}{2\pi}\right)^2 \frac{x^2}{(x^2+z^2)^2} \right]. \tag{11}$$

B. Hydrodynamic resistance force determination

In addition to the magnetic force $\vec{F}_m$ acting on the magnetic particles, there exists a viscous drag force $\vec{F}_s$ acting on the particle in the direction opposite to the particle motion.[33] This drag force, or Stokes force $\vec{F}_s$, is a function of the suspension medium viscosity (η), the radius of the particle (R_p), and the velocity $\vec{v}$ of the particle in the direction of the magnetic force. The inertial effects on the particles suspended in the fluid are negligible, as the Reynolds number is less than unity due to the geometric constraints of the microfluidic chamber. This result implies that while the fluid exerts drag on each particle, the particles exert no force on the fluid.[41,42] Furthermore, the number of particles within the suspension is assumed dilute, thus there exists no short-range interparticle dipolar interaction. As the magnetic particle is carried by the flowing solution in the $\hat{y}$-direction, within the context of laminar flow, the hydrodynamic forces only act in the $\hat{x}$-direction (direction perpendicular to flow). This force can be expressed as

$$\vec{F}_s = -6\pi\eta R_p v\hat{x}. \tag{12}$$

C. Joule heating

Resistive heating of the wires with respect to time ($\dot{q}$), or Joule heating, may limit the applied current range and geometry of the wires. Furthermore, this effect can adversely affect the flow and character of the fluid and may even degrade the device, rendering it nonreusable. Joule heating is determined by both the current conductor geometry and by the time duration of the applied current;[40] the heat generated in this manner is given by

$$\dot{q} = I^2 R. \tag{13}$$

Assuming no dissipative cooling, the electric resistance is equal to $R=\rho_R l_w/A$ for small wires, where l is the length of the wire, A is the cross-sectional area, and ρ_R is the electrical resistivity. This heat loss is dependent on the wire surface area, the thermal properties of materials of construction, and the properties of the ambient surroundings. Therefore, while current flow is constantly heating the wire as described in Eq. (13), the wire is simultaneously cooling through heat transfer to the surroundings (via radiation, convection, and conduction through its surface and to the surroundings). Although all three heat transfer phenomena are occurring simultaneously, most of the energy transfer is via conduction through the substrate containing the wires and through the microfluidic device above the wires. Hence, the general Fourier's law of heat conduction equation (or heat loss) appropriate for this situation is that mimicking an anisotropic medium, which is given as

$$k_x\frac{\partial^2 T}{\partial x^2} + k_y\frac{\partial^2 T}{\partial y^2} + k_z\frac{\partial^2 T}{\partial z^2} + \dot{q} = \rho_M C_p\frac{\partial T}{\partial t}, \tag{14}$$

where k_x, k_y, and k_z are the thermal conductivities of the substrate in the $\hat{x}$-, $\hat{y}$-, and $\hat{z}$-directions, respectively, $\dot{q}$ is the heat generation term (or Joule heating), and ρ_M and C_p are the density and heat capacity of the substrate, respectively.

Under the assumption that the width and length of the substrate are much larger than the height, the heat transfer in the $\hat{x}$- and $\hat{y}$-directions can be ignored, thus $dT/dx=dT/dy=0$. Combining Eqs. (13) and (14) yields

$$-k_z\frac{\partial T}{\partial z} = \dot{q}_0 g(t) f(x), \tag{15}$$

where $g(t)$ defines the time varying characteristics of the current that generates the heat, $f(x)$ is a spatial function that defines the wire locations along the $\hat{x}$-direction, and q_0 is the Joule heating provided at a reference current. Both $g(t)$ and $f(x)$ are controlled by the current characteristics and wire geometry, respectively. It should be noted that for the case of direct current, $g(t)=1$ and $\dot{q}_0=\dot{q}$. To complete the problem statement, it is assumed that the initial temperature is set equal to room temperature (298 K). To obtain the steady-state solution for a set temperature rise as a function of current, I, and wire cross-sectional area, A, a classical Fourier series method is needed. As this calculation is well established and is beyond the scope of this paper, details of the exact solution can be found in Ref. 43.

For the Joule heating calculation, the following physical characteristics are assumed for the device. Briefly, the overall layout of the cell separation device consists of a thick poly(dimethylsiloxane) (PDMS) slab bound to a thin glass coverslip, which is mounted on thin current-carrying copper wires deposited on a printed circuit board (PCB) substrate (Fig. 3). Traditionally, PCB copper wire arrays are mounted onto substrates composed of a material known as FR-4, which is a woven fiberglass cloth bound with an epoxy resin. For the purposes of this device model, the thermal conductivities of the PDMS (Ref. 44) and FR-4 (Ref. 45) were assumed to be equal to 0.2 W $(\text{m K})^{-1}$ and of equal thickness (1.5 mm), with the thermal resistance of the glass coverslip

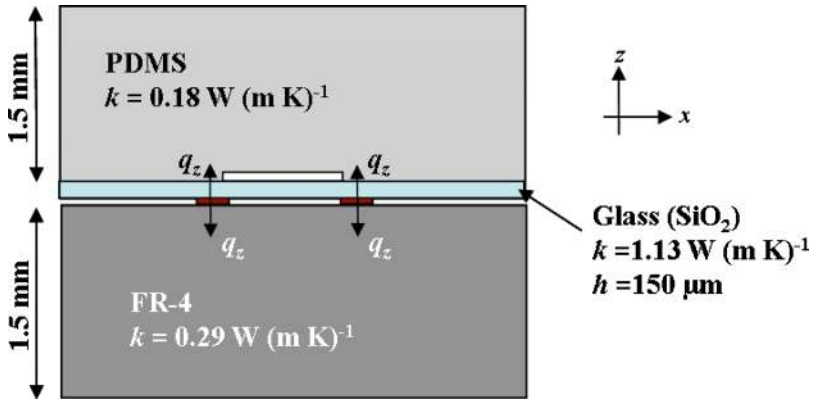

FIG. 3. Schematic illustration of cross sectional of printed circuit board electromagnetic array along with PDMS microfluidic device used in the evaluation of Joule heating constraints within rational device design. First both FR-4 and PDMS assumed to have thermal conductivity of ~0.2 W (m K)$^{-1}$ and heat transfer assumed in the z-direction only. The glass coverslip employed in the investigation is only 150 μm thick (h), and assuming minimal contact with air, thermal resistance above copper wires (brown) is assumed equal to PDMS alone.

ignored. Solving Eq. (15) at the steady-state condition, the current-carrying capacity, or the maximum current $I_{\max}$, which results in a specified temperature increase, was computed to be approximately $I_{\max}=2$ A for a nominal temperature rise of 20 K and for a standard PCB copper wire array cross section of 35 μm $\times$ 178 μm. Therefore, in the present experimental setup, Joule heating only becomes a concern at high currents ($I>2$ A) and/or if the wire cross-sectional area is significantly reduced.

IV. OPTIMIZATION OF THE CHANNEL LENGTH DEVICE DESIGNS

Utilizing the viscous drag $\vec{F}_s$, magnetic force $\vec{F}_m$, and Joule heating results obtained from earlier sections, it is now possible to explore the performance of the device subjected to realistic parameter values. It is desired to create a microfluidic cell separation device that delivers the greatest lateral displacement in the shortest possible channel, i.e., maximize x and minimize channel length l_{ch}. The overall force on the magnetic particle is the sum of the magnetic force $\vec{F}_m$ (Sec. III A) and the hydrodynamic force $\vec{F}_s$ (Sec. III B) that lends a constant velocity to the particle, which explicitly sets the acceleration equal to zero,

$$\vec{F}_m + \vec{F}_s = 0. \tag{16}$$

Equation (16) yields the overall equation representing the force in the x-direction exerted on a magnetic particle,

$$-\frac{V_p \chi_p}{\mu_0}\left[\left(\frac{\mu_0 I}{2\pi}\right)^2 \frac{x^2}{(x^2+z^2)^2}\right] - 6\pi\eta R_p v_x = 0. \tag{17}$$

The force balance can now be rearranged and solved for an optimized channel geometry to obtain a magnetophoretic microfluidic device design under the assumption of a fully developed fluid flow.

A. Generation I microfluidic device design

Rearranging Eq. (17) and assuming spherical geometry for the magnetic particles $\left(V_p = \frac{4}{3}\pi R_p^3\right)$ allows the determination of the velocity $\vec{v}$, normal to the magnetic field $\vec{B}$, in the $\hat{x}$-direction, of a magnetic particle flowing in the device channel. This process also allows an

estimate of the time t for the particle to traverse a given distance across the device channel width. In accordance with the geometry of the system, the velocity of the particle in the $\hat{x}$-direction is provided as

$$v_x = \frac{\mathrm{d}x}{\mathrm{d}t} = -\frac{R_p^2 \chi_p \mu_0 I^2}{18\eta\pi^2}\left[\frac{x}{(x^2+z^2)^2}\right]. \tag{18}$$

Reiterating, the variables in Eq. (18) are as follows: R_p is the radius of the magnetic particle, χ_p is the volumetric susceptibility of the particle, I is the current applied to the wire, η is the viscosity of the carrier solution, and z is the gap distance fixed by the glass coverslip. It should be noted that realization of an actual microfluidic magnetophoresis device requires the successful attachment of a large number of magnetic particles to the target cells in order to convey the largest magnetic moment possible the traveling complex. In the case of such a cell-particle complex, the above analysis is altered slightly to account for the drag forces on the cell itself, a body that is one to two orders of magnitude larger than the microparticles alone, depending on the actual tagging cell-particle characteristics. Therefore, for this case the viscous drag force on the cell-particle complex is now calculated using the larger cell radius (R_c), allowing the magnetic particle radius to be neglected ($R_c \gg R_p$). As previously described by Chalmers *et al.*,[46] the actual magnetic force exerted on a labeled cell derived from the magnetic field of the current-carrying wire is equal to the magnetic force on one particle [as described in Eq. (11)] multiplied by the number of particles attached to the cell ϕ, or $\vec{F}_m \cdot \phi$. Substitution of these parameters into Eq. (18) allows an estimate for the displacement time of the cell-particle complex out of the stream into the buffer fluid, attracted to the current-carrying wire

$$v_x = \frac{\mathrm{d}x}{\mathrm{dt}} = -\frac{R_p^3 \phi \chi_p \mu_0 I^2}{18 R_c \eta\pi^2}\left[\frac{x}{(x^2+z^2)^2}\right]. \tag{19}$$

The above differential equation may be solved analytically to obtain a solution of the form $x = f(t)$, where $f(t)$ is the residence time of a cell of radius R_c of the microfluidic chamber. In this manner, the lateral displacement x in the device of the magnetic cell-particle complex for any given value of time t can be calculated. This quantitative estimation of the physical parameters of the cell-particle complex flowing in a laminar fashion through the designated microfluidic device allows the determination of the optimal dimensions of the device. In particular, specification of the cell-particle complex displacement time t required to traverse the channel width w permits the determination of the minimum length (l_{ch}) of channel. Input of specific known parameters, such as the input volumetric flow rate ($\dot{V}$) of the carrier fluid, the device channel height (h), and width (w) of the carrier fluid stream, leads to calculation of the optimum length of the proposed device. The calculated residence time t may then be translated to a calculation of the lengthwise displacement l_{ch} of the cell-particle complex as the volumetric flow rate, $\dot{V}$, is given by

$$\dot{V} = \frac{V}{t} = \frac{l_{\mathrm{ch}} \cdot w \cdot h}{t}, \tag{20}$$

where l_{ch} represents the distance traveled along the channel along the $\hat{y}$-direction (lengthwise). Again, the microfluidic device design objective is to deliver the greatest lateral displacement in the shortest possible channel or, in other words, to maximize x while minimizing l_{ch}. To this end, the solution of Eq. (20) for residence time t and subsequent incorporation of Eq. (19) yields a relationship for the lateral particle displacement as a function of the distance traveled along the channel, $x = f(l_{\mathrm{ch}})$, under the influence of an applied magnetic field, with the trajectory provided below

$$\frac{\mathrm{d}x}{\mathrm{d}l_{\mathrm{ch}}} = -\frac{R_p^3 \phi w h \chi_p \mu_0 I^2}{18 R_c \dot{V} \eta\pi^2}\left[\frac{x}{(x^2+z^2)^2}\right]. \tag{21}$$

B. Generation II microfluidic device design

To determine the resultant magnetic field generated by the two conducting strips in the generation II design, improving upon the single-wire design of generation I, an array of conductors is considered where one conductor is positioned at far-edge of the microfluidic channel with current flowing in the negative $\hat{y}$-direction and the other conducting wire at the alternate edge of the microfluidic channel with current in the positive $\hat{y}$-direction, as shown in Fig. 2. The magnetic field components at any point (x,z) resulting from current flowing through the two conductors, set a distance equal to $2X$ apart, are given as

$$B_x(x,z) = B_x^o(x-X,z) - B_x^o(x+X,z), \tag{22a}$$

$$B_z(x,z) = B_z^o(x-X,z) - B_z^o(x+X,z), \tag{22b}$$

where B_x^o and B_z^o are the field components determined for the single-wire (generation I) configuration as specified in Eqs. (8a) and (8b) (as described in Sec. III A). Insertion of Eqs. (22a) and (22b) into the magnetic force equation [Eq. (9)] yields the expression for the magnitude of the attractive force exerted on a magnetic particle in the double-wire sheath (generation II) device design configuration,

$$F_{m,x} = \frac{V_p \chi_p}{\mu_0}\left[(B_x(x-X,z) - B_x(x+X,z))\left(\frac{\partial}{\partial x}\{B_x(x-X,z) - B_x(x+X,z)\}\right) + (B_z(x-X,z) - B_z(x+X,z))\left(\frac{\partial}{\partial z}\{B_x(x-X,z) - B_x(x+X,z)\}\right)\right]. \tag{23}$$

Substituting this new equation into Eq. (16), which describes the overall force balance and rearranging as outlined above in Eqs. (18)–(21) yields an equation for displacement as a function of channel length in the double-wire (sheath) device design

$$\frac{\mathrm{d}x}{\mathrm{d}l_{\mathrm{ch}}} = \frac{R_p^3 \phi w h \chi_p \mu_0 I^2}{18 R_c \dot{V} \eta \pi^2}\left[\left(\frac{z}{(x-X)^2+z^2} - \frac{z}{(x+X)^2+z^2}\right)\left(-\frac{2z(x-X)}{[(x-X)^2+z^2]^2} + \frac{2z(x+X)}{[(x+X)^2+z^2]^2}\right) + \left(-\frac{(x-X)}{(x-X)^2+z^2} + \frac{(x+X)}{(x+X)^2+z^2}\right)\left(\frac{(x-X)^2-z^2}{[(x-X)^2+z^2]^2} - \frac{(x+X)^2-z^2}{[(x+X)^2+z^2]^2}\right)\right]. \tag{24}$$

The resultant differential equation cannot be solved analytically. However, a solution of the form $l_{\mathrm{ch}}=f(x)$ can be obtained by numerical integration using the fifth-order Runge–Kutta method and appropriate solver software, such as MATLAB®. The results of this calculation are presented in Sec. VI B.

To reinforce the advantages of the two-wire array (i.e., generation II) in accordance with the derived equations, it can be shown that by adding one additional wire to the array increases the magnetic force by at least a factor of 4. Using Eq. (3) and the geometry illustrated in Fig. 2, it can be seen that the magnitude of the magnetic field $\vec{B}$ would be doubled, increasing the magnetic force $\vec{F}_m$ by a factor of 4. Additionally, the optimized geometry of the device results in a reduction of the displacement distance x and thus, intuitively, allows a further decrease in the required channel length l_{ch} versus that provided by the generation I design.

V. EXPERIMENTAL METHODS FOR QUANTIFICATION OF KEY DEVICE PARAMETERS

The derivation of the motion of a cell-particle complex in the described microfluidic design must be completed by determination of realistic values for applicable parameters within the mathematical expressions. To this end, the attainment of reasonable values for cell radius (R_c), magnetic susceptibility (χ), and particle binding characteristics (ϕ) was achieved via experiments conducted on a breast cancer cell line that served as a model for metastatic tumor cells. Dynabeads® MyOne™ superparamagnetic microbeads (Invitrogen, Carlsbad, CA) were used as

the model tagging particles to bind to the cells. These beads are composed of highly cross-linked polystyrene with superparamagnetic magnetite nanoparticles embedded within their matrices. The microbeads are coated with carboxylic acid (–COOH) groups that allow for the conjugation of biomolecules to their outer surface. According to the manufacturer, the magnetic particle diameter is 1.05 ± 0.03 μm ($R_p = 0.525 \pm 0.015$ μm), the magnetic mass susceptibility is 85×10^{-5} m^3 kg^{-1}, and the density is 1800 kg/m^3, which corresponds to a volume magnetic susceptibility $\chi = 1.5$. An approximate particle concentration value of $(7-12) \times 10^9$ particles/ml of stock particle suspension was also provided by the manufacturer. However, it should be noted that all these parameters may vary across lots and must be validated experimentally, as described below, to ensure a realistic rational device design. Quantitative results of the key parameters necessary to determine the device performance are provided in the last part of this section.

A. Model cell culture conditions and characteristics

MCF-7 human breast adenocarcinoma cells (ATCC, Manassas, VA) were cultured in 75 cm^2 tissue culture flasks at 37 °C in a humidified atmosphere with 5% CO_2 and 95% air. The cells were incubated in Eagle's Minimum Essential Medium (EMEM; ATCC) supplemented with 10% fetal bovine serum, 100 U ml^{-1} penicillin, 100 μg ml^{-1} streptomycin, and 0.01 mg ml^{-1} bovine insulin. Cells were grown to preconfluence and isolated for experiments by trypsinization using a 0.25% trypsin-Ethylenediaminetetraacetic (EDTA) solution.

The average cell radius was determined via electronic volume using a Coulter counter (Cell Laboratory Quanta™ SC; Beckman Coulter, Brea, CA) and compared to size-calibration beads (Flow-Check™ Fluorospheres; Beckman Coulter). The resulting average radius was also validated by bright-field microscopy with manual assessment of the radius of a number of the cells.

B. Magnetic particle diameter and characteristics

The magnetic microbead radius was determined via field emission-scanning electron microscopy (FE-SEM) (Hitachi S4800, Peoria, IL) of a dried particle suspension. Dried stock suspension was mounted on aluminum stubs and sputter-coated with gold-palladium to ~2 nm thickness to provide a connection path for electron density in FE-SEM examination. The experimentally determined particle concentration of the stock solution was verified against the concentration provided by the manufacturer. The stock suspension of particles was diluted 10 000 times and counted using a hemacytometer and a Nikon TE2000 inverted microscope employing Nikon Elements Advance Research software.

The magnetic susceptibility of the polymer/magnetite beads was confirmed via superconducting quantum interference device (Quantum Design MPMS XL-5, San Diego, CA) magnetometry. A 2 μl droplet of stock suspension was dried on a formvar-coated copper transmission electron microscopy grid (Electron Microscopy Science, Hatfield, PA). Magnetic hysteresis loops were measured at 300 K in the field range of -5 kOe $> H >$ 5 kOe. The moment of a blank grid was also measured and subtracted from the measured data; data were normalized to the mass of the particles. The magnetic character obtained from three replicates was averaged and the volumetric susceptibility was determined using the density values for the particles provided by Invitrogen.

C. Particle-cell attachment density

A binding assay was conducted to determine the number of particles that can attach to MCF-7 cells. DynaBeads® MyOne™ carboxylic acid particles were modified with antibodies against the epithelial cell adhesion molecule (anti-EpCAM; Santa Cruz Biotechnology, Santa Cruz, CA) using standard carbodiimide chemistry[47] in ratios suggested by the carbodiimide coupling reagent manufacturer (1:1 molar ratio of beads to protein; Pierce Biotechnology, Rockford, IL). Modified particles were incubated with approximately 1×10^6 cells for 30 min in 1 ml EMEM at concentrations of 0.1, 0.5, and 1 mg ml^{-1}. Following incubation, the cell-particle complexes were removed from suspension using a permanent magnet and were then incubated with a fluorescently labeled antibody against EpCAM (anti-EpCAM-FITC; Santa Cruz Biotechnology) for 30 min at a

TABLE I. Measured cell and particle characteristics for the determination of effective magnetophoretic displacement of cell-particle complex within microfluidic channel.

	Variable	Average	Error[a]	Units
Gap distance	Z	150	20	μm
Cell radius	R_c	7.5	1.3	μm
Particle radius	R_p	0.525	0.070	μm
Volumetric magnetic susceptibility	χ	1.10	0.19	a.u.
Binding density[b]	ϕ	794	280	particle cell^{-1}

[a]Standard deviation.
[b]Obtained from flow cytometry reading.

concentration of 1:100 (v/v). A cell suspension containing zero particles was also incubated with anti-EpCAM-FITC at the same concentration for comparison. In both cases, cells were separated from suspension via centrifugation at 190 × g for 5 min. The supernatant was retained and dried in order to assess the mass of the particles that remained after tagging, representing the unbound particles. All fluorescently tagged cells were resuspended in phosphate-buffered saline and subsequently analyzed for available receptor densities using a Beckman Coulter Quanta SC flow cytometry instrument. Results concerning the number of free receptors were compared with an antibody binding capacity calibration curve (Quantum™ MESF Beads; Bang Laboratory, Fishers, IN) to determine the initial number of available receptors on each cell (no particle attachment) and the number of receptors remaining after particle incubation (postparticle attachment). Comparison of the unbound particle mass, along with data obtained from untagged particle densities and the remaining receptor number after particle incubation, allows for the estimation of the average particle density on an individual cell.

D. Fabrication of a model validation device

To validate the developed optimized device design, microfluidic channels were fabricated as previously described.[48,49] To form the polymeric chambers, PDMS (Sylgard 184, Dow Corning, Midland, MI) elastomer was mixed (10:1 ratio) and poured onto a negative master, degassed, and allowed to cure overnight. PDMS replicas were then removed; inlet and outlet holes were punched with a 19G blunt-nose needle. Replicas and glass coverslips (60 (L) × 24 (W) × 0.15 (H) mm^3) were then exposed to oxygen plasma and placed in contact to bond irreversibly.

Wire arrays were designed using PCB123® printed circuit board design software and ordered from Sunstone Circuits (Mulino, OR). The wire dimensions were set to provide a gap encompassing the width of the device microfluidic channel; the height and width of the all of the wires were set to 35 and 178 μm, respectively. Teflon-insulated 18G copper wires were soldered to the ends of each of the printed circuit board arrays and the arrays were connected to a dc power supply (Elenco Electronics XP-4, Wheeling, IL) that provided three fixed-current setting at 0.25, 0.50, and 1.00 A via standard alligator clip connectors. The PDMS channels and wire arrays were visually aligned, followed by injection of a prepared homogenous MCF-7 cell suspension using a syringe pump (Harvard Apparatus, Holliston, MA).

VI. RESULTS AND DISCUSSION

A. Quantitative determination of key device parameters

To ensure a robust microchannel device, several measurements of each parameter were performed to obtain meaningful values for key parameters associated with the proposed device designs. These average values are presented in Table I. The average cell radius was determined to be $R_c = 7.5 \pm 1.3$ μm, which compares well with the previously reported radius values for the MCF-7 cell line [7.5–15 μm (Ref. 50)]. The average microbead particle radius was determined

via SEM to be 0.525 ± 0.050 μm, consistent with the manufacturer's specifications of 0.525 ± 0.015 μm. Furthermore, the volumetric magnetic susceptibility was determined to be 1.10 ± 0.19, comparable to the manufacturer's reported value of 1.5.

Approximation of the particle binding density per cell, ϕ, was then investigated. Under the ideal circumstances of complete surface area coverage of the cell surface, the maximum binding density of magnetic microparticles to one cell is determined to be 816 ± 161 particles/cell. However, determination of the actual particle binding character of the cell must consider biological characteristics such as the number of possible binding sites (i.e., receptors) available on the cell surface and clustering of these binding sites. To this end, the determination of the number of receptors available on the cells was conducted via flow cytometry analysis. A cell suspension was incubated with the fluorescently labeled antibody against EpCAM, a known antigen found on carcinoma cells and subsequently analyzed via flow cytometry to yield a receptor number of $251\,250 \pm 51\,382$ (approximately $\pm 20\%$) EpCAM binding sites per cell, comparable to previous reports of $222\,100 \pm 13\,700$ EpCAM receptors per cell.[50] A second suspension of cells (26.25×10^4 total cells) was then incubated with magnetic particles functionalized with anti-EpCAM at a concentration of 1 mg ml^{-1} for 30 min; the tagged cells were then removed via centrifugation. A concentration of 1 mg ml^{-1} magnetic microbeads in EMEM was demonstrated from flow cytometry experimentation with various particle suspensions to provide the maximum number of particles binding onto the cells. To ensure complete separation of the cells from the magnetic beads in suspension, centrifugation of the entire suspension was performed. Centrifugation ensures that all cells in suspension (untagged and tagged) will be subsequently analyzed, while separating free magnetic microparticles from the bound cells. The cells recovered following centrifugation were incubated with anti-EpCAM-FITC, which will bind to any free, unoccupied receptors remaining on the cell. These suspended cells were then analyzed for the number of available receptors free of particles. After incubation, the number of unoccupied EpCAM receptors was 6898 ± 1218 EpCAM antigens/cell, which equates to an approximate 97% antibody coverage and an overall binding density of 794 ± 280 microparticles/cell. To provide an independent confirmation of this value, the unbound microparticle suspension remaining after the centrifugation step was dried and weighed. A mass analysis was carried out, where the initial mass of particles that was incubated with 26.25×10^4 cells was 1.1 ± 0.1 mg and the remaining mass of cells after was determined to be 0.9 ± 0.1 mg. As determined by hemacytometry, the approximate microparticle concentration of particles per ml of liquid stock is $(8.45 \pm 1.33) \times 10^9$ particles ml^{-1}, which translates to $(8.45 \pm 1.33) \times 10^8$ particles/mg of dry magnetic microparticles. Therefore, by mass conservation, a particle binding density of 644 ± 338 beads/cell was determined, which is nearly 20% smaller than the coverage determined by flow cytometry but may be accounted for by dilution errors, hemacytometer errors, and the inaccuracies of the balance. However, comparison of the results attained from flow cytometry and mass conservation calculations illustrates that, within the margin of error, these two techniques yield consistent binding densities. This information is used to provide realistic constraints to the design of the microfluidic isolation device. Furthermore, understanding the distribution in cell radius, magnetic microbead particle radius, and binding densities ensures that the resulting device is sufficiently robust enough to isolate all the cells of interest.

B. Microfluidic device design optimization

Employing the expression derived in Sec. IV for the displacement of a cell-magnetic particle complex under the influence of a magnetic field and utilizing the values derived in Sec. V, Table I, for the key parameters in the expression, it is now possible to computationally investigate the physical behavior and appropriate dimensions of the generation I and generation II cell separation device designs. Solving Eq. (20) for the length l_{ch} of the generation I device with a reasonable lateral cell-particle complex displacement (Δx) of 100 μm and employing the commercial microbeads described earlier indicates that the applied current (I) would need to be greater than 10 A to produce a field sufficient to ensure that the length of the channel l_{ch} remained below 1 m. Not only is this applied current value well above the constraints set by minimizing the Joule heating

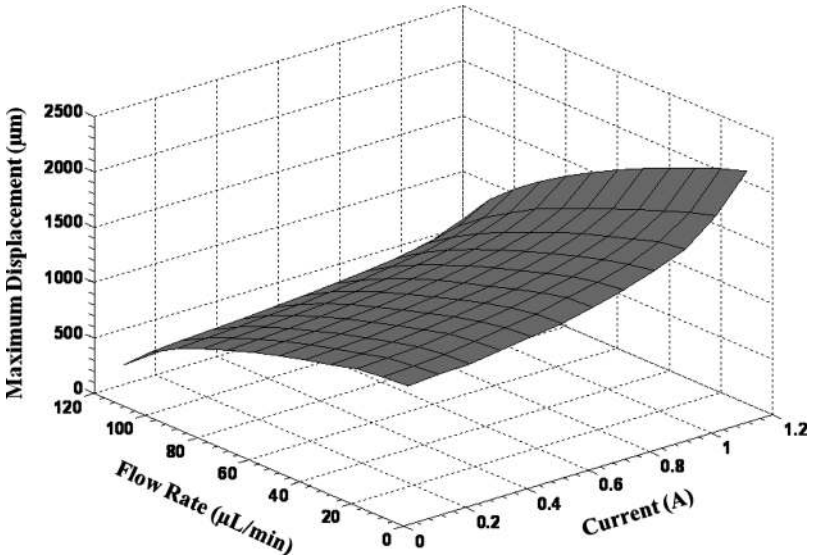

FIG. 4. Surface plot illustrating maximum displacement achievable as a function of volumetric flow rate (μl min^{-1}) and current (a) derived in Eq. (24). All parameters fixed at average values in Table I and the length of the device is constrained to 50 mm. Current varied from 0.1 to 1.2 A and volumetric flow rate varied from 10 to 120 μl min^{-1}. Maximum displacement increases with increasing current and decreases with increases in the flow rate.

contribution, the derived device length of 1 m is unrealistic. This result motivated the generation II design, as derived in Eq. (24), which was designed to (i) reduce the device length required for cell displacement and isolation relative to the generation I design and (ii) increase the magnetic forces experienced by the tagged target cells by virtue of its double current-carrying wire design that produces double the magnetic field. An average maximum cell displacement for the generation II device, using the earlier-described parameters, was determined from Eq. (24); as before, the intended design was envisioned to consist of a disposable microfluidic component and a reusable electromagnetic component, with the length of the device set by the length of commercially available glass slides (60 mm). To compute the lateral displacement of the cell-particle complex in the device, two current-carrying wires of equal dimension are placed at the outer edges of the device, the height of the channel (h) is assumed to be 50 μm, and the distance between the channel midpoint and the current-carrying wire array is set equal to the thickness of a #1 glass slide ($z=150$ μm). This lateral displacement was determined as a function of current and volumetric flow rate using a rearrangement of Eq. (24). Volumetric flow rates are directly impacted by changes in channel width or starting position of the cell-particle complex; therefore, derivation of the cell-particle complex displacement as a function of volumetric flow rate is nonlinear and these two variables must be solved simultaneously in the calculation. It should be noted that the calculated complex displacement is defined as the distance from the outside edge of the channel, near the wire, to the long axis of the microfluidic channel [Fig. 2(c)]; therefore, the width of the channel is equivalent to twice the displacement, as shown in Fig. 2(c).

The surface plot shown in Fig. 4 illustrates the maximum displacement of an average cell-particle complex from channel edge to channel center as a function of current I and volumetric flow rate $\dot{V}$ for the generation II device, as determined from Eq. (24). The displacement maxima, defined as the largest distances that the cell-particle complex traverses to reach the device center within a length of 50 mm, are below 2100 μm (or 2.1 mm), a width significantly less than that of a standard coverglass slide (24 mm). The device length was set to 50 mm to account for the integration of the channel outlet and inlets to create a hydrodynamic focusing of the buffer stream, as illustrated in Fig. 2(a). As expected, higher current through the device provides greater maxi-

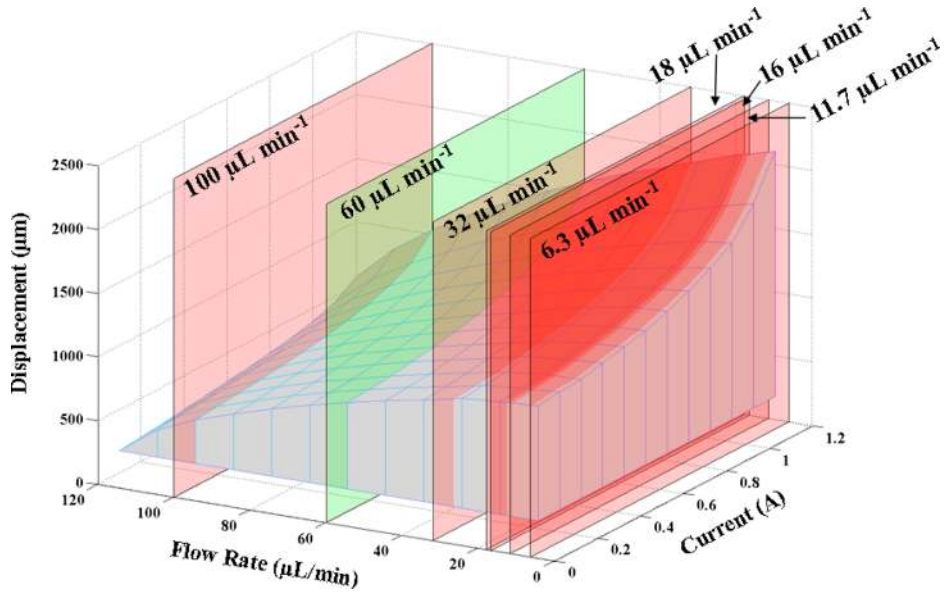

FIG. 5. The surface plot of displacement of cell-particle complex on standard glass coverslip (60 (L) × 24 (W) × 0.15 (H) mm) compared with current literature values of isolation of target cell populations. Intersecting planes drawn at average throughputs for commercial magnet-based separation (green; 60 μl min^{-1}) and microfluidic cell separation devices (red; 11.7–100 μl min^{-1}). The three-dimensional plot illustrates rational design yields comparable throughputs, and narrow channel widths allow for greater throughputs than state-of-the-art separators.

mum cell displacement, as the magnetic force increases as I^2. The linear velocity of the cell in the $\hat{x}$-direction increases with increasing volumetric flow rates, causing a less drastic displacement as the particle travels down the microfluidic channel ($\hat{y}$-direction).

Figure 5 depicts the surface plot from Fig. 4 along with intersecting planes that represent sample volumetric flow rates utilized with magnet-activated and nonmagnetic cell separation systems described in the literature. Other researchers who have isolated cells using commercial[9] or microfluidic[5,22,25,51–54] systems have employed volumetric flow rates on the order of 6.3–100 μl min^{-1}. Figure 5 illustrates that this simple design can effectively meet and exceed the processing speeds or throughputs of both commercial systems (green plane) and microfluidic devices (red planes). This is a relevant comparison for the present work because any new separation device must have at least the same throughput as similar, state-of-the-art systems. Furthermore, control of the applied current and channel widths in this device allows for cell throughputs higher than those currently reported in literature for other comparable devices.[5,22,25,51–54] Although the higher cell throughput provided by the current design is advantageous, it is still unclear what the anticipated effect of device parameters on purity of collected target cells will be as there remains a dearth of literature addressing the effect of flow rates on efficiency and purity of the isolated cell suspension from heterogeneous suspensions. A review of the literature on magnetic-bead-based device designs (both commercial and microfluidic designs) shows that no correlation between purity, efficiency, and flow rate has yet been illustrated. Therefore, to assess this relationship extensive experimental validation of the presented design with biologically relevant mixed cell populations is needed but this remains beyond the scope of the current study.

So far, all presented calculations were derived from average particle and cell characteristics shown in Table I, whereas distributions in the values of these particular parameters were not considered. To address these parameter variations, the cell and particle diameter distributions shown in Table I were factored into the computational device design. This analysis demonstrates a need to design the generation II system according to the lower bound of the maximum cell-particle complex displacement, as illustrated in Fig. 6, rather than target the average displacement of the complex, as described earlier (Figs. 4 and 5). To assess the worst-case scenario, or the

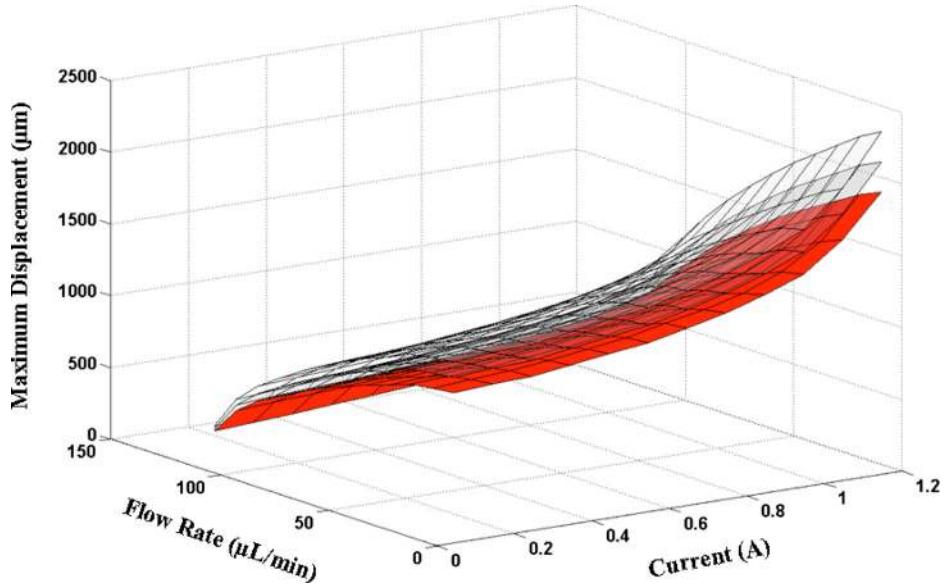

FIG. 6. Consideration of distribution in cell and particle parameters constrains the true maximum displacement achievable. The average maximum displacement in Fig. 4 replotted, shown at the center transparent white surface plot. The upper bound plot (as shown in transparent white) represents case of highly mobile cell-particle complex, i.e., small cells maximally labeled with magnetic particles or best-case scenario (R_p=0.595 μm, R_c=6.2 μm, ϕ=1074 particles cell^{-1}, and χ=1.29). The case where larger-than-average cells experience high drag and are tagged with small particles with low susceptibility with minimum binding density (i.e., worst-case scenario), shown in red, represents the true realistic parameter space (R_p=0.455 μm, R_c=8.8 μm, ϕ=514 particles cell^{-1}, and χ=0.91).

lowest maximum displacement, the least favorable bounds of each of the parameters were inserted into the design equation (i.e., R_p=0.455 μm, R_c=8.8 μm, ϕ=514 particles cell^{-1}, and χ=0.91). As it is desired that all cells be displaced from the sample stream into the collection stream located at the center of two sheath fluids (i.e., 100% recovery), the lower bound surface models the movement of a large cell with minimal magnetic-particle binding densities and thus minimal magnetic force experienced. Thus, the lowest surface plot shown in red in Fig. 6 represents the most conservative rational design criterion that should be followed for subsequent design of a magnetic-based cell separation platform.

The parametric analysis conducted in this study illustrates that particle binding characteristics, as well as the individual cell and particle properties, do play an integral role in the separation efficiency. Unfortunately, most commercial MACS systems have been generalized for the separation of a wide variety of cell population and are not tuned to account for these variations in particle-cell binding character. Therefore, this standardization of the commercial system may result in the low yields currently found for magnet-based cell isolations. Moreover, the total number of particles bound to a particular cell is a direct function of the cell type, the particle type, and the specific marker of interest. Therefore, prior to any experimentation, the number of particles bound to the cell ϕ must directly measured, as presented in Sec. VI A and subsequently included in the validation studies presented below. Ultimately, assessment of the effects of particle binding density, or poor labeling efficiency, on cell separation efficiency of the presented design requires future experimental validation with different cells populations.

Following the determination of the rational design criteria, preliminary validation studies of the sheath device were conducted with a homogeneous suspension of MCF-7 carcinoma cells in phosphate-buffered saline at a cell concentration of 1×10^5 cells ml^{-1}. Several combinations of applied current, flow rate, and channel widths were investigated. By selecting specific combinations of these three variables, it is possible to probe designs that should separate all cells (below the red surface plot in Fig. 6), designs that should not separate the cells (above the upper bound in Fig. 6), and design that should separate some of the cells (between the upper and lower bounds in

TABLE II. Capture efficiency for an initial cell concentration of 5×10^4 cells ml^{-1}. The efficiency was determined for three different microfluidic channel width (w=250, 500, and 1000 μm) injected at three different flow rates ($\dot{V}$=10, 50, and 120 μl min^{-1}) and influenced by an electromagnetic field at three different currents (I=0.25, 0.50, and 1.00 A).

	w=250 μm			500 μm			1000 μm		
$\dot{V}$	I=0.25 A	0.50 A	1.00 A	0.25 A	0.50 A	1.00 A	0.25 A	0.50 A	1.00 A
10 μl min^{-1}	93.0 ± 2.7	⋯	⋯	92.1 ± 1.6	⋯	⋯	12.7 ± 1.6	96.8 ± 5.7	96.8 ± 1.6
50 μl min^{-1}	97.7 ± 2.7	⋯	⋯	57.1 ± 7.3	⋯	⋯	8.1 ± 1.6	13.0 ± 4.3	92.7 ± 4.9
120 μl min^{-1}	97.0 ± 4.0	98.5 ± 10.6	97.0 ± 1.5	6.3 ± 4.2	76.2 ± 2.8	98.6 ± 1.6	1.6 ± 1.6	9.8 ± 2.8	45.5 ± 4.3

Fig. 6). As shown in Table II, the combinations predicted to separate all of the cells had efficiencies of approximately 100% within the margin of error, whereas combinations that forced the design outside of the optimized region yielded very low separation of labeled cells from the buffer solution. Interestingly, those parameters that intersect between the upper and lower bounds in Fig. 6 illustrate that only a percentage of the cells were actually separated from the fluid stream. Furthermore, as the parameter intersection approached the lower bound (or worst-case scenario), the percentage of cells increases toward 100% efficiency separation. This result illustrates that the surface plots shown in Fig. 6 accurately represent the available device design space, and given one or two parameters an optimized functional device can be attained. A second validation of the rational design was then probed as a means to test cell concentration influences on the efficiency of separation for a single set of device parameters. A device made with optimal design parameters, as determined from the model and experimental preliminary validation (w=250 μm, $\dot{V}$ =120 μl min^{-1}, and I=0.25 A), was employed to test the efficiency of cell isolation as a function of MCF-7 concentration in buffer (10–10 000 cell ml^{-1}). As shown in Fig. 7, in this instance the efficiency of cell separation remains around 100% as the total number of cells injected is lowered from 10 000 cells to as low as 10 cells. Overall, the results of these validation tests illustrate that the device design optimized according to the derived computational model can effectively isolate (~100%) of a magnetic-particle-tagged population of cells from a general cell suspension even in low abundance.

It should be noted that separation of a cell population from a homogenous cell suspension still remains too ideal to conclude that the presented device design optimization will successfully extend to a heterogeneous suspension. All biologically relevant cell suspensions have several additional factors that are anticipated to affect the separation characteristics of the device, such as cell-particle migration under shear conditions, flow and collision-induced aggregation, and unintentional labeling of nontarget cells with magnetic beads. Unfortunately, each of these factors is highly dependent on the properties of the suspension (e.g., cell-particle binding densities and carrier solution characteristics) and thus is difficult to generalize for the inclusion into the presented analysis.

Another question that has yet to be evaluated is the effect of concentration (target cell plus nontarget cell total) on the efficiency of target cell isolation. The recovery or yield of rare cell isolation (subpopulations of <1%)[15,55] techniques reported in literature for MACS systems over the past ten years remain too low (20%–80%)[56–61] for possible application in diagnostic medicine. A possible explanation of the low cell recoveries currently reported in literature may be a result of a lack of a rational optimization approach toward device design, which has been addressed within this investigation and/or the elastic collisions of cells within the heterogeneous suspension.[62] As the target cells move across the flow stream within the described design, there will be numerous collisions with neighboring cells, causing interference in the lateral displacement and possible deviation away from the displacement stream. As with flow rate effects on cell separation purity and efficiency, this effect must be evaluated via further experimental validation.

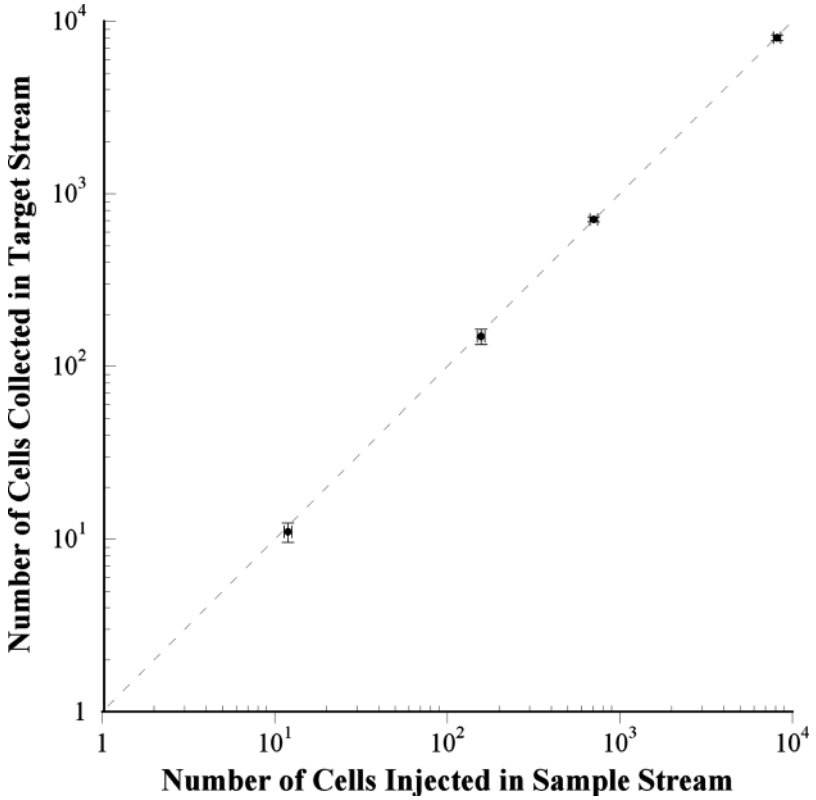

FIG. 7. The capture efficiency was shown to be nearly 100% for homogeneous samples of 10–10 000 MCF-7 cells injected. As determined from the experiments shown in Table II, all experiments were conducted with a 250 μm wide microfluidic channel at a flow rate of 120 μl min^{-1} and a current of 0.25 A. The four solid points represent five replicate experiments ($n=5$) for each respective cell suspension and the dotted line represents 100% efficiency of cell capture. Error bars represent the standard error of both the input cell number and the collected cell number ($n=5$).

VII. CONCLUSIONS

A mathematically based rational model is presented for the design of a magnet-activated microfluidic cell isolation device. The model is based on a first-principles force calculation for spherical, uniform cells labeled with superparamagnetic microbeads and is believe to be well-suited for the specific enrichment of rare cell populations from a sample stream. Two geometric layouts are investigated in this report. The first design incorporated a single current-carrying wire located adjacent to a microfluidic channel with simple straight channel geometry and a single displacement direction (Fig. 1). The second design considered two current-carrying wires with currents running antiparallel, allowing for displacement in both the negative and the positive lateral directions into a central buffer stream (Fig. 2). The two-wire array, with a hydrodynamic focusing of a separation stream, was shown to be preferable over the single-wire based design and allows for the complete separation platform to fit on a standard glass coverslip (60 (L) $\times$24 (W) $\times$0.15 (H) mm^3). Microbead and cell parameters, such as diameter, magnetic susceptibility, and particle binding characteristics, were experimentally determined and the resultant values directly inserted into the design equations to ensure realistic cell displacement estimates. Furthermore, key variables including current I and volumetric flow rate $\dot{V}$ were investigated and compared with those accompanying state-of-art separation devices currently available and described in literature. This work illustrates that effective displacement-based separation can be achieved with electromagnets driven by reasonable and tunable currents as opposed to the more expensive and constant field permanent magnet approaches currently in use. Overall, the proposed cell separation device design could serve as a valuable tool for continuous-flow cell separation

device design to the fields of diagnostic and regenerative medicine. Future work on magnetophoretic cell separation will focus on comparison and adjustment of the presented computational rational device design in comparison with the actual device performance with heterogeneous cell suspensions. Evaluation of the performance of the device utilizing heterogeneous cell suspensions will allow for the assessment of the minimum cell concentration that may be effectively separated from the cell population as well as the effect that cell concentration may have on the resulting efficiency and purity of the recovered target cell stream.

ACKNOWLEDGMENTS

The authors would like to thank Ernie Lewis of Brookhaven National Laboratory for assistance in mathematical formulations. This work was supported by the IGERT Nanomedicine and Science Program (Grant No. NSF-DGE-0504331), by NSF Grant No. 0932195, and by Northeastern University.

Nomenclature

h	Height
k	Thermal conductivity
l	Length
$\dot{q}$	Joule Heat
t	Time
w	Width
x	Distance
A	Cross-sectional area
B	Magnetic field
F	Force
I	Current
H	Coverslip height
L	Coverslip length
R	Radius
T	Temperature
$\dot{V}$	Volumetric flow rate
W	Coverslip width
χ	Susceptibility
η	Viscosity
μ_o	Permeability in vacuum
ρ_M	Density
ρ_R	Electrical resistivity
ϕ	Number of particle attached to cell

Subscripts

c	Cell
ch	Channel
inj	Injection
m	Magnetic
p	Particle
s	Viscous drag (Stokes law)
w	Wire
x	Vector in the x-direction
y	Vector in the y-direction
z	Vector in the z-direction

[1] M. Cristofanilli, G. T. Budd, M. J. Ellis, A. Stopeck, J. Matera, M. C. Miller, J. M. Reuben, G. V. Doyle, W. J. Allard, L. W. M. M. Terstappen, and D. F. Hayes, N. Engl. J. Med. **351**, 781 (2004).
[2] M. Hristov and C. Weber, Drug Discovery Today **5**, e267 (2008).

[3] M. Radisic, R. K. Iyer, and S. K. Murthy, Int. J. Nanomed. **1**, 3 (2006).
[4] J. V. Green and S. K. Murthy, Lab Chip **9**, 2245 (2009).
[5] S. Nagrath, L. V. Sequist, S. Maheswaran, D. W. Bell, D. Irimia, L. Ulkus, M. R. Smith, E. L. Kwak, S. Digumarthy, A. Muzikansky, P. Ryan, U. J. Balis, R. G. Tompkins, D. A. Haber, and M. Toner, Nature (London) **450**, 1235 (2007).
[6] R. Pethig, Biomicrofluidics **4**, 022811 (2010).
[7] N. Pamme, Lab Chip **7**, 1644 (2007).
[8] S. K. Murthy and M. Radisic, in *Encyclopedia of Microfluidics and Nanofluidics*, edited by D. Li (Springer, New York, 2008), pp. 202–208.
[9] D. D. Putnam, V. Namasivayam, and M. A. Burns, Biotechnol. Bioeng. **81**, 650 (2003).
[10] J. M. Hill, G. Zalos, J. P. J. Halcox, W. H. Schenke, M. A. Waclawiw, A. A. Quyyumi, and T. Finkel, N. Engl. J. Med. **348**, 593 (2003).
[11] R. R. Joseph and D. Belpomme, Lancet **1**, 747 (1975).
[12] J. Laurence and S. M. Astrin, Proc. Natl. Acad. Sci. U.S.A. **88**, 7635 (1991).
[13] R. P. Messner, Arthritis Rheum. **17**, 339 (1974).
[14] A. Thiel, A. Scheffold, and A. Radbruch, Immunotechnology **4**, 89 (1998).
[15] S. Miltenyi, W. Muller, W. Weichel, and A. Radbruch, Cytometry **11**, 231 (1990).
[16] J. J. Chalmers, M. Zborowski, L. P. Sun, and L. Moore, Biotechnol. Prog. **14**, 141 (1998).
[17] F. Carpino, L. R. Moore, J. J. Chalmers, M. Zborowski, and P. S. Williams, J. Phys.: Conf. Ser. **17**, 174 (2005).
[18] M. Berger, J. Castelino, R. Huang, M. Shah, and R. H. Austin, Electrophoresis **22**, 3883 (2001).
[19] D. W. Inglis, R. Riehn, R. H. Austin, and J. C. Sturm, Appl. Phys. Lett. **85**, 5093 (2004).
[20] D. W. Inglis, R. Riehn, J. C. Sturm, and R. H. Austin, J. Appl. Phys. **99**, 08K101 (2006).
[21] N. Pamme, J. C. T. Eijkel, and A. Manz, J. Magn. Magn. Mater. **307**, 237 (2006).
[22] N. Pamme and C. Wilhelm, Lab Chip **6**, 974 (2006).
[23] A. E. Saliba, L. Saias, E. Psychari, N. Minc, D. Simon, F. C. Bidard, C. Mathiot, J. Y. Pierga, V. Fraisier, J. Salamero, V. Saada, F. Farace, P. Vielh, L. Malaquin, and J. L. Viovy, Proc. Natl. Acad. Sci. U.S.A. **107**, 14524 (2010).
[24] S. S. Shevkoplyas, A. C. Siegel, R. M. Westervelt, M. G. Prentiss, and G. M. Whitesides, Lab Chip **7**, 1294 (2007).
[25] Y. Xu, J. A. Phillips, J. L. Yan, Q. G. Li, Z. H. Fan, and W. H. Tan, Anal. Chem. **81**, 7436 (2009).
[26] P. R. C. Gascoyne, J. Noshari, T. J. Anderson, and F. F. Becker, Electrophoresis **30**, 1388 (2009).
[27] N. Pamme, Lab Chip **6**, 24 (2006).
[28] B. Weigl, G. Domingo, P. LaBarre, and J. Gerlach, Lab Chip **8**, 1999 (2008).
[29] G. S. Fiorini and D. T. Chiu, BioTechniques **38**, 429 (2005).
[30] K. S. Kim and J. K. Park, Lab Chip **5**, 657 (2005).
[31] N. Pekas, M. Granger, M. Tondra, A. Popple, and M. D. Porter, J. Magn. Magn. Mater. **293**, 584 (2005).
[32] N. Xia, T. P. Hunt, B. T. Mayers, E. Alsberg, G. M. Whitesides, R. M. Westervelt, and D. E. Ingber, Biomed. Microdevices **8**, 299 (2006).
[33] R. B. Bird, W. E. Stewart, and E. N. Lightfoot, *Transport Phenomena*, 2nd ed. (Wiley, New York, 2002).
[34] S. Chandrasekhar, Rev. Mod. Phys. **15**, 1 (1943).
[35] T. H. Boyer, Am. J. Phys. **56**, 688 (1988).
[36] H. Lee, A. M. Purdon, and R. M. Westervelt, Appl. Phys. Lett. **85**, 1063 (2004).
[37] H. C. Hayes, Phys. Rev. **3**, 295 (1914).
[38] D. Melville, F. Paul, and S. Roath, IEEE Trans. Magn. **11**, 1701 (1975).
[39] A. C. M. Kuo, in *Polymer Data Handbook*, edited by J. E. Mark (Oxford University Press, New York, 1999), pp. 411–435.
[40] P. A. Tipler and G. Mosca, *Physics for Scientist and Engineers*, 5th ed. (Freeman, New York, 2004).
[41] A. Sinha, R. Ganguly, and I. K. Puri, J. Magn. Magn. Mater. **321**, 2251 (2009).
[42] A. Sinha, R. Ganguly, A. K. De, and I. K. Puri, Phys. Fluids **19**, 117102 (2007).
[43] Y. Ling, *Proceedings of the 52nd Electronic Components and Technology Conference*, San Diego CA, 2002 (IEEE, New York, 2002), pp. 1683–1693.
[44] H. Lobo and C. Cohen, Polym. Eng. Sci. **30**, 65 (1990).
[45] F. Sarvar, N. J. Poole, and P. A. Witting, J. Electron. Mater. **19**, 1345 (1990).
[46] J. J. Chalmers, Y. Zhao, M. Nakamura, K. Melnik, L. Lasky, L. Moore, and M. Zborowski, J. Magn. Magn. Mater. **194**, 231 (1999).
[47] G. T. Hermanson, *Bioconjugate Techniques* (Academic, Boston, 1996).
[48] B. D. Plouffe, D. Njoka, J. Harris, J. Liao, N. K. Horick, M. Radisic, and S. K. Murthy, Langmuir **23**, 5050 (2007).
[49] Y. N. Xia and G. M. Whitesides, Angew. Chem., Int. Ed. **37**, 551 (1998).
[50] N. Prang, S. Preithner, K. Brischwein, P. Goster, A. Woppel, J. Muller, C. Steiger, M. Peters, P. A. Baeuerle, and A. J. da Silva, Br. J. Cancer **92**, 342 (2005).
[51] A. A. Adams, P. I. Okagbare, J. Feng, M. L. Hupert, D. Patterson, J. Gottert, R. L. McCarley, D. Nikitopoulos, M. C. Murphy, and S. A. Soper, J. Am. Chem. Soc. **130**, 8633 (2008).
[52] J. P. Gleghorn, E. D. Pratt, D. Denning, H. Liu, N. H. Bander, S. T. Tagawa, D. M. Nanus, P. A. Giannakakou, and B. J. Kirby, Lab Chip **10**, 27 (2010).
[53] J. H. Myung, C. A. Launiere, D. T. Eddington, and S. Hong, Langmuir **26**, 8589 (2010).
[54] S. J. Tan, L. Yobas, G. Y. H. Lee, C. N. Ong, and C. T. Lim, Biomed. Microdevices **11**, 883 (2009).
[55] A. A. S. Bhagat, H. Bow, H. W. Hou, S. J. Tan, J. Han, and C. T. Lim, Med. Biol. Eng. Comput. **48**, 999 (2010).
[56] T. Schneider, S. Karl, L. R. Moore, J. J. Chalmers, P. S. Williams, and M. Zborowski, Analyst (Cambridge, U.K.) **135**, 62 (2010).
[57] R. M. Shenkman, J. J. Chalmers, B. J. Hering, N. Kirchhof, and K. K. Papas, Tissue Eng. Pt., C-Meth. **15**, 147 (2009).
[58] G. Y. Wang, Y. Li, Y. M. Yu, B. Yu, Z. Y. Zhang, Y. Liu, and S. J. Wang, J. Gastroenterol. Hepatol **24**, 299 (2009).
[59] D. J. Richel, H. E. Johnsen, J. Canon, T. Guillaume, M. R. Schaafsma, C. Schenkeveld, S. W. Hansen, I. McNiece, A. J. Gringeri, R. Briddell, C. Ewen, R. Davies, J. Freeman, S. Miltenyi, and M. Symann, Bone Marrow Transplant **25**, 243 (2000).

[60] J. A. Cancelas, S. Querol, G. Martin-Henao, C. Canals, C. Azqueta, J. Petriz, J. Ingles-Esteve, and J. Garcia, Pure Appl. Chem. **68**, 1897 (1996).
[61] L. S. Wong, W. J. Bateman, A. G. Morris, and I. A. Fraser, Br. J. Surg. **82**, 1333 (1995).
[62] M. R. King, S. D. Rodgers, and D. A. Hammer, Langmuir **17**, 4139 (2001).